The observed signature of mesoscale eddies in sea surface temperature and the associated heat transport

Ute Hausmann*, Arnaud Czaja

Imperial College London, Department of Physics, Space & Atmospheric Physics Group, SW7 2BW London, UK

ABSTRACT

An estimate of the signature of mesoscale motions in sea surface temperature (SST) is provided for the North Atlantic and the Southern Ocean by analysing the relationship between satellite microwave SST and multi-altimeter sea surface height (SSH) observations. After a preliminary analysis at fixed location, the study focuses on the SST/SSH relationship following eddy tracks.

At fixed location, the clearest signature of mesoscale motions in SST is found in regions of large SSH variability, roughly coincident with the major fronts of the Gulf Stream and the Antarctic Circumpolar Current (ACC). Large-scale, likely atmospherically forced, variability masks a major part of the mesoscale signature in SST in more quiescent parts of the World Ocean.

Following eddy tracks allows us to detect the signature of mesoscale motions in SST even in regions of weak SSH variability. The track-following analysis reveals robust westward phase shifts of the eddies' SST anomalies with respect to their rotating cores in all regions. In energetic regions, the observed intense warm-top anticyclones and cold-top cyclones are only nearly in-phase, whereas in quiet regions, weaker SST signatures are almost in quadrature with the eddies' SSH.

Propagating eddies are found to flux heat poleward in the mixed-layer over a broad range of oceanic regimes and the size of this heat transport is particularly significant in the ACC region (≥ 0.2 PW). Although eddy shedding from major currents is appealing as a mechanism for heat transport ("drift" heat transport), we find that the poleward (equatorward) motion of warm anticyclones (cold cyclones) produces a much weaker poleward heat transport in the mixed layer than that resulting from the westward phase shift between SST and SSH fluctuations ("swirl" heat transport). Associated diffusivities, modest in quiescent interiors ($\kappa < 1000$ m^2 s^{-1}), intermediate in the ACC (1200 m^2 s^{-1}) and large in the Gulf Stream ($\simeq 3000$ m^2 s^{-1}), thus primarily reflect the eddy swirl heat transport.

1. Introduction

The oceanic mesoscale (≈ 100 km) features vigorous currents and associated instabilities which are instrumental in setting the ocean's stratification (e.g. Rhines and Young, 1982) and contribute to the poleward heat transport of the climate system (Jayne and Marotzke, 2002; Marshall et al., 2002; Voorhis et al., 1976; Wunsch, 1999). The *quasi-stationary* component of these circulations, that is, what remains after multi-year averaging, is known to possess strong thermal surface expressions in the form of narrow fronts in sea surface temperature (SST). These are observed to be strongly coupled to the atmospheric boundary layer (Chelton et al., 2004; Small et al., 2008; Song et al., 2004; Sweet et al., 1981) and possibly exert an impact on the atmosphere far above the boundary layer (Czaja and Blunt, 2011; Minobe et al., 2008; Song et al., 2006).

In contrast, the signature in SST of the *transient* component of the mesoscale field, the focus of this paper, is only starting to be systematically established from observations. Whereas an SST signal is expected as a dynamical part of surface-intensified baroclinic eddies, the association is less clear at high-latitude, where salinity is important in shaping the eddy mixed-layer density anomaly; it is also less clear for barotropic eddies. Moreover, the eddy SST signature could be quickly eroded by turbulent air–sea heat exchanges, as a result of the expected enhancement of the negative heat flux-SST feedback towards smaller scales (Bretherton, 1982; Rahmstorf and Willebrand, 1995).

A multitude of studies from satellite infra-red observations have described the presence of mesoscale anomalies in SST, primarily in the form of energetic "rings" spawned by the Gulf Stream (e.g. Auer, 1987; Brown et al., 1986; Cornillon et al., 1989; Halliwell and Mooers, 1979; Park et al., 2006; Richardson et al., 1979; Ring Group, 1981), but also in the Southern Ocean (Lentini et al., 2002). However, due to the sparseness of in-situ observations, it has not always been possible to make an explicit connection

* Corresponding author. Tel.: +44 20 7594 1402; fax: +44 20 7594 7900.
E-mail address: uh07@imperial.ac.uk (U. Hausmann).

between the observed surface thermal anomalies and the eddying flow field. Satellite altimetry has increased our knowledge and the observational coverage of mesoscale circulations at the sea surface, but early attempts to link satellite-based sea surface height (hereafter SSH) and SST variability have necessarily been limited by the low resolution capacities of mono-mission altimetry and homogeneous infra-red datasets ($\geq 1°$, see for example the studies by Cipollini et al., 1997; Halliwell et al., 1991; Leeuwenburgh and Stammer, 2001).

The combination of satellite altimetry and in-situ data has provided invaluable insight into the temperature and velocity distribution of mesoscale motions. Using repeated XBT measurements along a route from San Francisco to Honolulu to Guam to Taiwan, and the SSH observations from the Topex-Poseidon altimeter, Roemmich and Gilson (2001) were able to demonstrate a systematic westward phase tilt of temperature fluctuations with decreasing depth by averaging over more than 400 mesoscale "eddies". Similar results were found south of the Kuroshio by Qiu and Chen (2005) using temperature profiles from Argo floats, through-cloud microwave (MW) observations of SST, and by taking advantage of the improved SSH resolution offered by multi-mission altimetry.

In this study, we wish to further extend the surface analysis reported by Qiu and Chen (2005) south of the Kuroshio to different regions (the Gulf Stream, the Antarctic Circumpolar Current and quiet parts of the subtropical gyres) by taking advantage of the automated eddy tracking algorithm developed recently by Chelton et al. (2011b, hereafter referred to as CSS11), which provides more than 1200 eddy tracks per year in the regions considered here. By averaging SST fluctuations along these tracks, we are able to isolate a statistically robust signature of transient mesoscale motions in SST and compute the associated poleward heat transport in the mixed layer.

After a description of observational datasets and methods (Section 2), we isolate the signature of transient mesoscale motions in SST by analysing the SST-SSH relationship observed both at fixed-location (Section 3) and following eddy tracks (Section 4). In Section 5 we discuss the implications for poleward heat transport, before summarizing our conclusions in Section 6.

2. Data and methods

A global long-term study of the mesoscale contribution to SST variability has become possible with the launch, in June 2002, of the Advanced Microwave Scanning Radiometer (AMSR-E). With the drawback of a relatively large footprint that limits its effective resolution to ≈ 50 km (Chelton and Wentz, 2005), it provides near-daily global SST observations through clouds. This greatly reduces data gaps and the resulting need for spatio-temporal smoothing compared to traditional clear-sky only infra-red observations. Here we use version 2 of the optimally interpolated MW SST dataset, provided by Remote Sensing Systems (REMSS) on a daily, $\frac{1}{4}°$ grid.

Microwave SSTs are normalized to represent daily-minimum ocean skin temperatures (Gentemann et al., 2003). Although these closely represent bulk SST, defined as the vertically homogeneous temperature of the mixed-layer, small differences (usually less than 0.2 K) may occur. In the Southern Ocean, seasonal biases between AMSR-E and in-situ observations of bulk SST are however observed to closely average out in the annual mean (Dong et al., 2006). To first approximation, AMSR-E SST can therefore be assumed to be representative of the mixed-layer, whose depth is approximated here by the $2° \times 2°$ monthly climatology of de Boyer Montégut et al. (2004).

Anomalies in SST (hereafter SSTA) are constructed by removing the observed mean-state and seasonal cycle, estimated by averaging all observations available at a given location and day of year over the June 2002 to December 2007 period studied. The main drawback of constructing the seasonal cycle in this empirical way is that, as explained in detail in Appendix A, it biases towards lower values our estimate of the eddy SST anomaly (estimated at $(n-1)/n \approx 0.8$ of its true observed value, where n is the number of years considered).

Regarding sea surface height, we use the near-real time dynamic topography provided by AVISO every 3–7 days on a $\frac{1}{3}°$-Mercator grid. This multi-altimeter product merges data from at least three altimeter missions (4 in the sub-period October 2002 to September 2005), which has been shown to greatly enhance the accurate resolution of mesoscale features in SSH in comparison to mono-mission datasets (Ducet and Le Traon, 2000; Pascual et al., 2006; CSS11). For consistency, sea surface height anomalies (SSHA) are constructed in the same way as SSTA by the removal of their background seasonal climatology, estimated from merged altimeter data after linear interpolation onto a daily time-grid. (For the correlation analyses with SSTA presented below, a small remaining temporal mean and a linear trend are also removed from both anomaly datasets, and SSHA are linearly interpolated onto the $\frac{1}{4}°$ SST grid).

Finally, we will use the global dataset of observed mesoscale eddy tracks (with lifetimes of at least 4 weeks and amplitudes of at least 1 cm) described in detail by CSS11. It is obtained by an automated algorithm that identifies and follows eddies as closed contours in spatially high-pass filtered SSH (retaining scales smaller than $20°$ longitude, $10°$ latitude). Eddies tracked in this way originate nearly everywhere in the world's ocean and partition into roughly equal numbers of cyclones and anticyclones (characterized respectively by lows and highs in sea level) with average amplitudes of ≈ 10 cm, radii of ≈ 100 km and lifetimes of ≈ 6 months. Note that the SSHA used here differs in dataset as well as method (seasonal cycle removed) from those used by CSS11 to track eddies (spatially high-pass filtered).

## 3. The observed SST-SSH relationship at fixed location

A measure of the spatial scales of SSTA observed in the North Atlantic (NA) and the Southern Ocean (SO) is provided in Fig. 1a,b, respectively. Spatial correlations are defined, at each grid point, as the average over spatial lags of the (zero time-lag) SSTA autocorrelation matrix, up to maximum lags of $\pm 2.5°$ longitude and $\pm 1°$ latitude. In the Tropics and quiescent interiors of ocean basins, high correlations are found (red shades, in Fig. 1a,b), indicating coherent SSTA signals over the $5° \times 2°$ scale used. In contrast, in the Antarctic Circumpolar Current (ACC) and western-boundary current extensions like the Gulf Stream (GS) system and the Brazil-Malvinas Confluence (BMC) lower values (blue shades) indicate characteristic SSTA scales much smaller than $5° \times 2°$.

The same calculation is shown for the sea surface height anomalies in Fig. 1c (NA) and Fig. 1d (SO). SSHA scales are observed to be much smaller than $5° \times 2°$ nearly everywhere (blue shades, in Fig. 1c,d), suggesting a widespread presence of intense mesoscale circulations. Large-scale SSHA (red shades, in Fig. 1c,d), likely reflecting steric height anomalies within the upper mixed layer, predominate only in very high and low latitudes of the NA and in several "eddy-deserts" of the SO (CSS11).

Over the bulk of the regions with a clear presence of mesoscale circulations (blue shades, in Fig. 1c,d), characteristic SSTA scales are much larger than mesoscale (red shades, in Fig. 1a,b). This suggests that in these regions the signature of mesoscale circulations in SST is masked by other processes, such as large-scale air–sea interactions
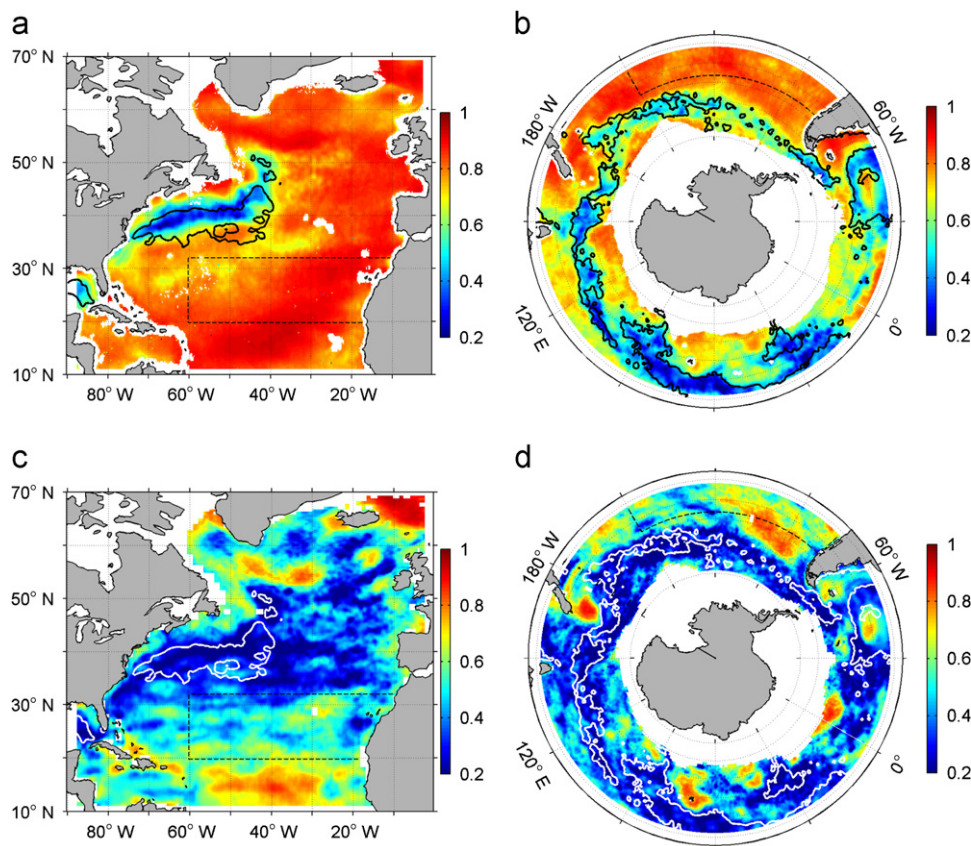
Fig. 1. Observed spatial correlations of SSTA (a,b) and SSHA (c,d) for NA (a,c) and SO (b,d), averaged over boxes of $5° \times 2°$. Energetic regions are indicated by the thick contour of SSHA rms (15 cm in NA, 10 cm in SO, black in a,b, white in c,d), quiescent subtropical regions by the dashed boxes, as discussed in Section 3. See text for details of the calculation of spatial correlations. (For interpretation of the references to colour in this figure, the reader is referred to the web version of this article.)
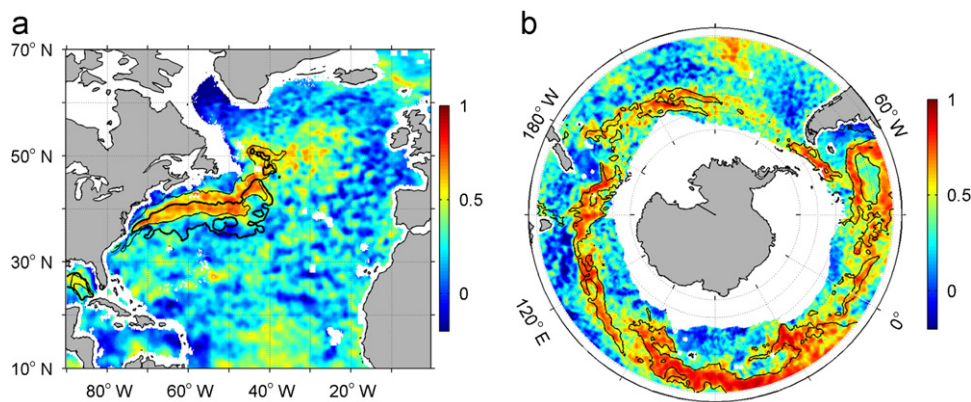
Fig. 2. Simultaneous cross-correlation between SSTA and SSHA for NA (a) and SO (b). The thin black contour delimits regions of intense mesoscale isotherm stirring, where the rms of anomalous geostrophic background SST advection exceeds 1.5 K/10 days in the NA and 1 K/10 days in the SO. For the NA, the 15 cm SSHA rms contour (thick) is repeated from Fig. 1.

in the form of anomalous air–sea heat exchange and anomalous Ekman advection (e.g. Frankignoul, 1985). Interestingly, however, SSTA and SSHA scales become comparable in regions of high SSHA standard deviations, σ_{SSHA}, associated with strong current systems and intense mesoscale variability. In these regions, outlined by the thick black contour in Fig. 1 (15 cm σ_{SSHA} contour in NA, 10 cm in SO), one therefore expects to be able to detect the signature of mesoscale eddies in SST much more easily than anywhere else.

Further analysis of the relationship between SSTA and SSHA is provided in Fig. 2, which displays the instantaneous cross-correlation between the two fields. The correlation is found to be weak in quiet oceanic interiors but, as expected from the previous discussion,

larger in regions of higher σ_{SSHA} (locally exceeding 0.7 in the NA and 0.8 in the SO – note that correlations are also relatively high at a few locations in the eddy-deprived areas mentioned above, where they reflect large-scale signals in SSHA and SSTA).

Over the GS, the region of high correlations in Fig. 2a and low correlations in Fig. 1a is shifted slightly to the north of the highest σ_{SSHA} (thick black contour). Indeed, here, sea surface height variability peaks along the warm tongue of SST created by the GS, where it cannot impact the mixed-layer heat budget through horizontal advection due to the absence of a background temperature gradient. A mesoscale SSTA signature is instead more clearly observed along the strong SST front marking the North

Wall of the separated GS, where anomalous geostrophic SST advection[1] typically exceeds 1.5 K/10 days (indicated by the thin black contour in Fig. 2a). Along the ACC, in contrast, regions of large σ_{SSHA} coincide more closely with surface fronts and therefore, with regions of large geostrophic advection (the 1 K/10 day contour is given in Fig. 2b, to be compared with the 10 cm contour of σ_{SSHA} in Fig. 1b).

In summary, Eulerian statistics suggest that a clear signature of mesoscale circulations in SST should be detected in regions of large eddy stirring of background isotherms. These regions will be referred to as "energetic" in the following, and will simply be singled out using a threshold contour of σ_{SSHA} (15 cm for NA and 10 cm for SO). Detecting the SST signature of mesoscale circulations in other parts of the ocean is more challenging and we will in the following focus on two such regions, referred to as "quiescent": the eastern parts of the subtropical gyres in the North Atlantic and South Pacific (defined here as the regions east of 60°W, 20–32°N and east of 150°W, 40–48°S, as indicated by the dashed boxes in Fig. 1).

4. The observed SST-SSH relationship following eddy tracks

To estimate the signature in SST of mesoscale eddies with origins in the "energetic" and "quiescent" regions defined above, we now turn to an analysis of the SST following the tracks of eddies in SSHA, as provided by CSS11 (cf. Section 2).

4.1. "Energetic" regions

A large number of mesoscale eddies with origins in the energetic GS and ACC regions are tracked over the period studied (532 for the GS and 3782 for the ACC). Although their average tracked lifetime is between 3 and 4 months, they can live up to 3 years, and, in a typical week, around 25 of them coexist in the GS region, and more than 160 along the ACC (not shown). This results in over 25,000 weekly snapshots of both anticyclones and cyclones, for which weekly mean SSTA and SSHA data (obtained as described in Section 2), centred on the eddy position in time and space, are evaluated. To establish a characteristic SSTA signature of eddies in energetic regions, track-following composite maps of eddy SSTA and SSHA are constructed by averaging over all of the weekly snapshots, along all eddy tracks.[2]

The resulting composites are presented in Fig. 3a,b, and reveal a very clear signature of GS and ACC eddies in sea surface temperature and sea surface height. Near-isotropic rotating cores are seen in this average, with typical SSHA amplitudes of ≈ 15 cm (in contours). Within these cores, anticyclones are associated with warm SSTA, cyclones with cold SSTA, both with typical amplitudes of ≈ 0.75 K (in colour). This in-phase relationship between SSHA and SSTA is consistent with the strong correlations seen in Fig. 2. Warm/cold eddy cores are surrounded by weaker amplitude, negative lobes in both height and temperature anomalies. These are reminiscent of wave-like (meander) structures or may be indicative of densely packed eddies in these energetic regions.

The averaging involved in the construction of eddy composites conceals important SSTA fluctuations between individual eddy events. Indeed, standard deviations of SSTA between eddy snapshots have the same order of magnitude as the average signal in Fig. 3a,b

(not shown), implying that a given SSTA snapshot does not always reveal the presence of an eddy—a fact highlighted in previous studies (e.g. Halliwell and Mooers, 1979) In the light of these large fluctuations, a *t*-test provides an indication of the statistical significance of the observed composite SSTA signature. Even after reducing the number of degrees of freedom from the number of eddy events to the number of tracks, to account for correlations, observed composite SSTA is shown to be significantly different from zero at the 99% confidence level throughout the eddy cores and lobes. (The significance is only found to fall below the 99% confidence level (dotted in Fig. 3) in the transition region between positive and negative values.)

A closer inspection of Fig. 3 reveals that eddy SSTA and SSHA are not exactly in phase. For both anticyclones and cyclones, maximum SSTA occur slightly to the west of eddy maxima in SSHA. Over anticyclones, maximum SSTA are also shifted slightly poleward, and over cyclones, slightly equatorward. Zonal and meridional sections through the centre of the eddy composites (Fig. 3c,d) clearly show these phase shifts, and indicate that they are typically on the order of the local deformation radius ($R_d \approx 20$ km, as indicated by the dashed lines in Fig. 3a–d, and obtained by averaging the deformation radii calculated by Chelton et al. (1998) over the energetic regions).

To test whether this shift is statistically significant, we have repeated the composite analysis over several subsets of the original data (GS, SO, short and long lived eddies as indicated in Table 1). Despite resulting differences in SSTA amplitudes, subset-based composites all reveal a systematic westward shift, in the same direction as observed in the all-eddy composite, on the order of the local deformation radius, or $\approx 1/5$ of the eddy radius. In addition, we have also tested whether SSTA on the east side of the eddy ($x > 0$) were significantly different from SSTA on the west side ($x < 0$) of the eddy[3] by producing, rather than a composite for SSTA(x) as in Fig. 3, a composite for SSTA(x)-SSTA(-x). As can be seen in Fig. 4, western and eastern eddy SSTA are statistically different from each other at the 99% confidence level everywhere within the eddy cores (dotted elsewhere, calculated using a *t*-test as in Fig. 3a,b) for both anticyclones (Fig. 4a) and cyclones (Fig. 4b). The slight westward phase shift between the surface temperature and pressure of an eddy is thus a robust feature of the observations used here.

4.2. "Quiescent" regions

In quiescent regions composites of SSTA and SSHA are produced in the same way as described above for energetic eddies – more than 1500 and 1000 eddies originating in the interior of the South Pacific and North Atlantic, respectively, were followed for this purpose. Composites are displayed separately for anticyclones and cyclones in Fig. 5a,b. The composite of SSHA is similar in shape and radius to that of the energetic eddies (Fig. 3a,b), but its amplitude (< 5 cm) is reduced by more than a factor of 4. The SSTA composite reveals a systematic but rather weak signature (reduced by a factor of 5 compared to the eddies' in energetic regions), with warm anomalies stronger over anticyclones and cold anomalies stronger over cyclones. Compared to Fig. 3a,b though, the SSTA signature is markedly more bipolar, and almost in quadrature with SSHA, rather than primarily in-phase. Although the anomalies in Fig. 5a,b are smaller than those in Fig. 3a,b, a *t*-test shows these features to be statistically significant at the 99% level.

The phase shifts in both zonal and meridional directions are much larger in Fig. 5a,b than in Fig. 3a,b. This is clearly seen in the zonal and meridional sections through the composites provided

---

[1] This process is estimated from the data as $\vec{v}'_g \cdot \vec{\nabla}\overline{T}$, in which $\vec{v}'_g$ is the geostrophic velocity anomaly estimated from SSHA using the geostrophic relation, and $\vec{\nabla}\overline{T}$ is the gradient of the long-term mean SST field.

[2] Before averaging, individual snapshots of SSTA and SSHA are normalized by the instantaneous eddy radius, which is defined by CSS11 as the radius of maximum rotational eddy speed and is typically on the order of 80 km. A normalized grid spacing of $\frac{1}{5}$ eddy radii is chosen, which is comparable or slightly smaller than the $\frac{1}{4}°$ AMSR-E SST resolution.

[3] The eddy centre is defined by the eddy position in CSS11's dataset and observed to coincide with the maximum in composite SSHA. East and west refer to distances x along a constant latitude from that centre.
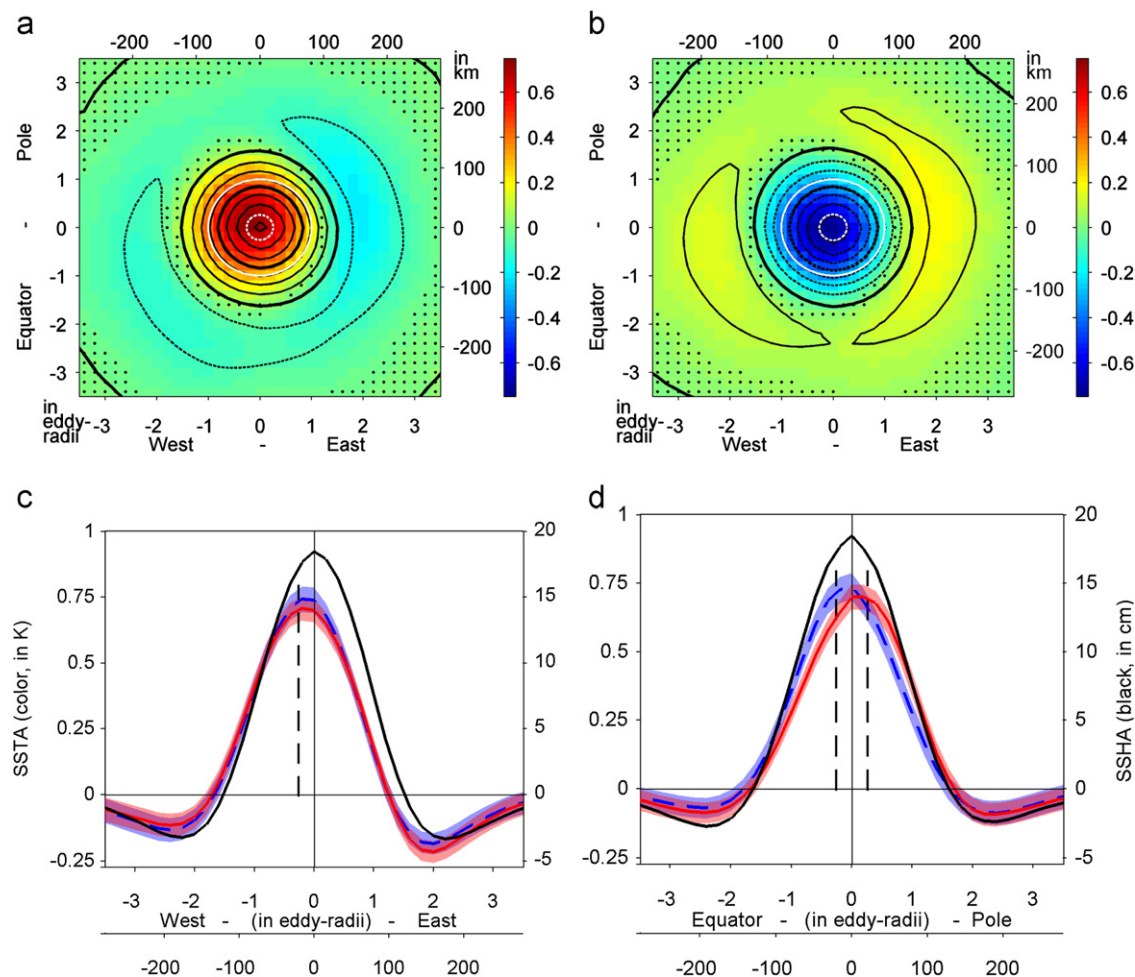
Fig. 3. Track-following composites of energetic regions' eddy SSTA and SSHA. Maps for anticyclones (a) and cyclones (b) colour SSTA and contour SSHA (every 2.5 cm with 0 & 10 cm in thick, negative values dotted). Zonal (c) and meridional (d) sections through the eddy centre highlight phase shifts of SSTA (red-continuous/blue-dashed for anticyclones/cyclones, cyclonic sections multiply by −1) compared to SSHA (black, for weighted both-polarity average). A composite *t*-test (see text for details of the statistics) indicates where SSTA are significantly different from zero at the 99% confidence level (non-dotted areas in a,b), the corresponding confidence intervals are shaded in the eddy SSTA sections (in c,d). Composites are normalized onto an eddy-radius grid (unit-circle in white), but composite average deformation radius (dashed in all panels) and absolute scales (km) are shown for reference. (For interpretation of the references to color in this figure caption, the reader is referred to the web version of this article.)

Table 1
Variability of the observed westward phase shift.

|	Energetic			Quiet		
	ALL	GS	ACC	ALL	NA	SP
ALL	0.73/−0.2	0.76/−0.2	0.72/−0.2	0.15/−0.6	0.10/−0.6	0.19/−0.6
A	0.71/−0.2	0.65/−0.4	0.72/−0.2	0.16/−0.6	0.10/−0.8	0.20/−0.6
C	0.74/−0.2	0.88/−0.2	0.72/−0.2	0.14/−0.6	0.10/−0.6	0.18/−0.6
short	0.69/−0.2	0.69/−0.2	0.69/−0.2	0.11/−0.6	0.05/−0.6	0.14/−0.6
long	0.76/−0.2	0.82/−0.2	0.75/−0.2	0.18/−0.6	0.13/−0.8	0.23/−0.6

Value/position of the maximum SSTA (in K/in eddy radii) along the east–west section through the centre of the composite over all eddies within the indicated groups. A: anticyclones, C: cyclones, short/long: eddies with lifetimes ≤ / > 16 weeks, NA: North Atlantic, SP: South Pacific, ACC: Antarctic Circumpolar Current.

in panels c and d of the Figures. Indeed, the systematic westward zonal phase shift is observed to reach more than half of the eddy radius *r* in quiet regions (or 1.5 times the local deformation radius). Table 1 indicates that this result holds for all subsets of the eddies considered, with maximum SSTA consistently shifted to the west of eddy centres by about 0.6 *r*.

4.3. Link to previous studies

Apart from studies following rings in infra-red SST observations, which all implicitly assume an in-phase relationship between temperature and pressure fluctuations (Auer, 1987; Brown et al., 1986; Lentini et al., 2002), there exists, to our knowledge, no systematic track-following analysis of eddy SSTA signatures close to the world's major current systems and associated vigorous eddy fields. We thus compare our results with those published previously in regions of weak and moderate eddy activity.

During the MODE experiment in the North Atlantic, phase shifts between eddy surface and subsurface temperature fields were observed by Voorhis et al. (1976) in the subtropical convergence zone, a region of intermediate eddy activity. Later, several analyses of fixed-location SSTA and SSHA observations (exploiting spatio-temporal lag correlations and coherence analysis of wavenumber-frequency spectra), have, with the exception of Cipollini et al. (1997), all detected westward phase shifts of mesoscale SSTA centres with respect to pressure centres. Low-resolution observations show relatively large phase shifts at larger scales (wavelengths ≈ 800 km) than those studied here (composite eddy wavelengths vary between 400 and 600 km), again for regions of intermediate eddy activity (Halliwell et al.,
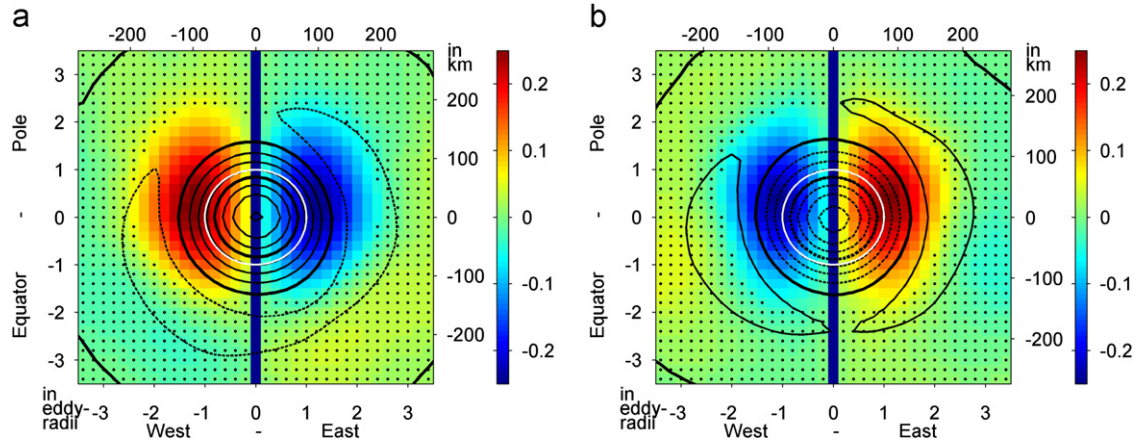
Fig. 4. Zonal asymmetry of energetic regions' eddy SSTA composite: (a) anticyclones and (b) cyclones. Non-dotted areas indicate where eastern and western composite SSTA are significantly different from each other at the 99% confidence level. Otherwise, apart from a different colour-scale for the zonal SSTA difference, same as Fig. 3. (For interpretation of the references to color in this figure caption, the reader is referred to the web version of this article.)
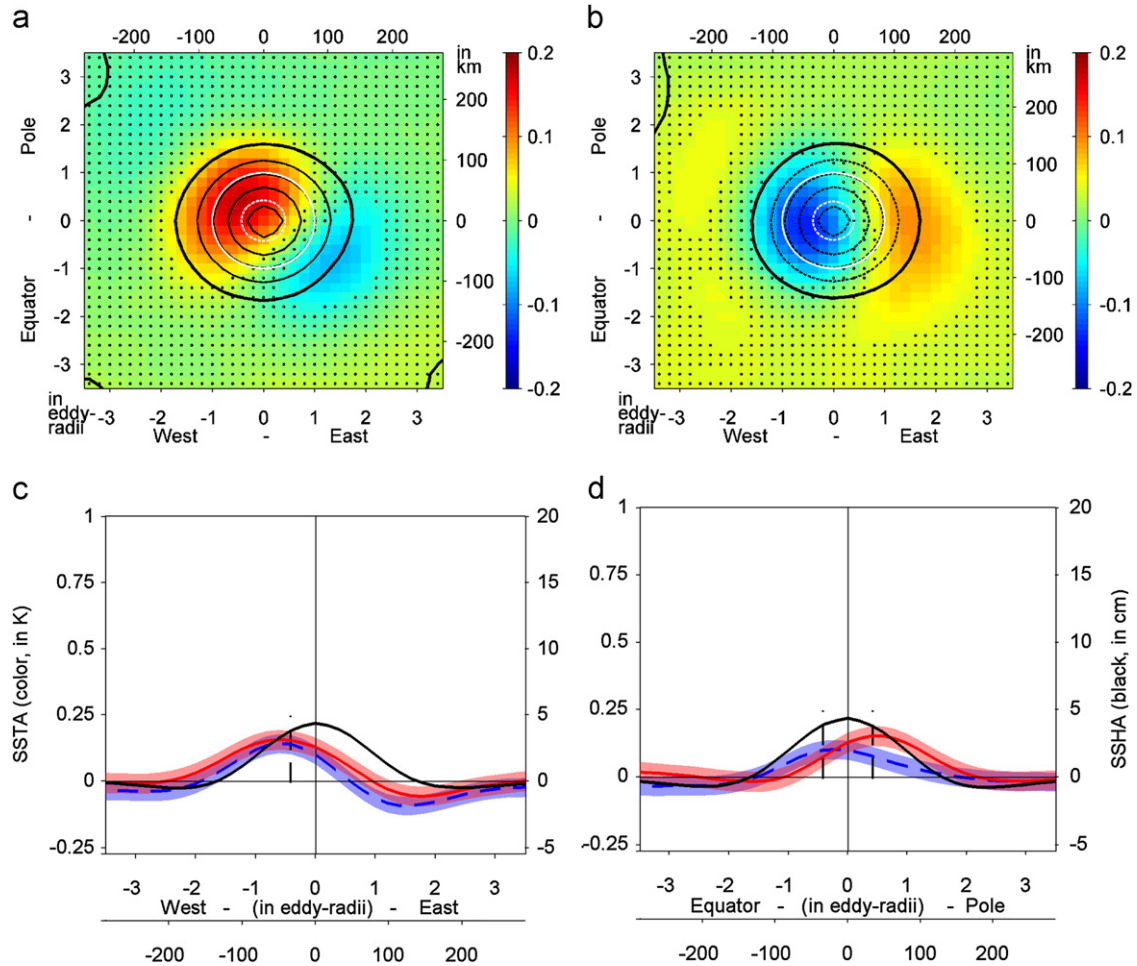
Fig. 5. Track-following composites of quiet region eddy SSTA and SSHA. Note the different SSTA colour-scale ($\pm$.2 K) and SSHA contour-intervals (1 cm, with 0 & 5 cm in thick) compared to the composite of energetic regions' eddies, otherwise same as Fig. 3. (For interpretation of the references to color in this figure caption, the reader is referred to the web version of this article.)

1991) and in a global analysis (Leeuwenburgh and Stammer, 2001). The latter study furthermore finds evidence of decreasing shifts with increasing latitude.

In the Pacific, Qiu and Chen (2005) detect phase shifts between SSH and SST fluctuations on the order of the deformation radius between 20°N and 40°N, which in terms of magnitude, compare well with our observations. However, their analysis of the temperature

and velocity structure through depth in two eddies sampled by ARGO floats, just south of the Kuroshio, show westward phase shifts larger than the eddy radius r near the surface. The latter are consistent in direction, but not in magnitude, to those observed here, but it is important to emphasize the very small sample size of Qiu and Chen (two eddies) compared to ours (≥ 2500 in quiet and ≥ 4200 in energetic regions). It is possible that this discrepancy

reflects a contamination of the mesoscale SST signal in Qiu and Chen (2005) by large scale processes, while our much larger sampling allows us to average out such effects. Finally, in a comprehensive study of over 410 intense eddy events detected in a repeat transect through regions of weak to moderate eddy activity, Roemmich and Gilson (2001) observe phase shifts of 0.4° longitude for eddy radii r of 1° longitude. This corresponds to a westward phase shift of $\frac{2}{5}r$ in regions of moderate eddy activity, which is between our findings of shifts larger than $\frac{1}{2}r$ (typically $\frac{3}{5}r$) in quiet regions, and smaller than $\frac{1}{2}r$ (typically $\frac{1}{5}r$) in energetic regions.

5. Eddy mixed-layer heat transports

5.1. Framework for estimating heat transports

At a given latitude y, the poleward heat transport H throughout the mixed layer across a zonal extent L_x is given by

$$H(y) = \int_0^{L_x} \rho_o c_p h_{ml} v T \, dx, \qquad (1)$$

where $\rho_0 = 1025 \text{ kg m}^{-3}$ is an average density, $c_p = 4000 \text{ J kg}^{-1} \text{ K}^{-1}$ is the specific heat capacity of seawater, v is the meridional velocity and T is the temperature averaged over the mixed layer of depth h_{ml}.

Propagating mesoscale features contribute to H through correlations between the perturbations they induce in temperature, δT, and meridional velocity, δv. These occur if coherent meridional eddy movements (with velocities v_d) are accompanied by a systematic difference in δT between poleward and equatorward drifting eddies. This gives rise to a component of H referred to in the following as "drift heat transport". Correlations between δT and $(\delta v - v_d)$, which occur if there is a temperature difference between the poleward and equatorward moving sides of each individual eddy, give rise to a component of H which we will refer to as the "swirl heat transport" in the following.

To quantify these two components we consider what (1) would be if a single eddy contributed to the heat transport. To do so we decompose the temperature and velocity field into a background, or environmental component, and a perturbation associated with the eddy:

$$T = T_{env} + \delta T \quad \text{and} \quad v = v_{env} + \delta v. \qquad (2)$$

Since we are considering the case where only the eddy contributes to the heat transport, we write $v_{env} = 0$ and $H = \delta H$. Further introducing the meridional drift velocity v_d of the eddy crossing the latitude in question by writing $\delta v = v_d + (\delta v - v_d)$, the contribution of a single eddy to (1) becomes:

$$\delta H = \int_0^{L_x} \rho_0 c_p h_{ml}(\delta v - v_d) T \, dx + \int_0^{L_x} \rho_0 c_p h_{ml} v_d T \, dx = \delta H_{swirl} + \delta H_{drift}. \qquad (3)$$

The time-averaged net contribution of propagating mesoscale eddies to H is then obtained by summing (3) over all eddies $n(t)$ crossing L_x at a given time, and averaging in time:

$$H = \overline{\sum_{i=1}^{n(t)} \delta H(i)} = \overline{n} \langle \delta H \rangle, \qquad (4)$$

where $\langle \, \rangle$ denotes the composite average over all eddies at all times, and the overline denotes the time-average. Similarly, the two components of heat transport can be written as:

$$H_{swirl} = \overline{n} \langle \delta H_{swirl} \rangle \quad \text{and} \quad H_{drift} = \overline{n} \langle \delta H_{drift} \rangle. \qquad (5)$$

The requirement of zero time-average perturbation flow across L_x, $\langle \delta v \rangle = 0$, by noting that the swirl component of the flow $(\delta v - v_d)$ is non-divergent across each eddy, implies that $\langle v_d \rangle = 0$ (which could simply reflect the same number of eddies drifting poleward and

equatorward across L_x on average). This allows us to rewrite (5) as:

$$H_{swirl} = \overline{n} \left\langle \int_0^{L_x} \rho_0 c_p h_{ml}(\delta v - v_d) \delta T \, dx \right\rangle + \epsilon \qquad (6)$$

and

$$H_{drift} = \overline{n} \left\langle \int_0^{L_x} \rho_0 c_p h_{ml} v_d \delta T \, dx \right\rangle + \epsilon, \qquad (7)$$

as terms involving T_{env} vanish (to a residual ϵ due to correlations between δv and differences in T_{env} between individual eddies, which is neglected in the following).

We now apply (6) and (7) to observations, using the composites produced in the previous section, to isolate the eddy perturbations δT and δv, and using the eddy tracks as a proxy for the eddy drift velocity v_d. Note that several further approximations need to be made before doing so. Firstly, contributions to H_{swirl} by correlated inter-eddy fluctuations around the eddy average δT and δv will not be computed (e.g., $\langle \delta v \delta T \rangle$ will be replaced by $\langle \delta v \rangle \langle \delta T \rangle$). Furthermore, the mixed-layer depth in the above equations will be approximated by its large-scale seasonal climatology $\overline{h}_{ml}$, which is evaluated and composite-averaged along eddy tracks. From the feedback of eddy δT on turbulent air–sea heat fluxes and thus convection (Dewar, 1986; Williams, 1988), eddy perturbations in mixed-layer depth are expected to be of opposing sign over anticyclones (enhanced air–sea heat loss and convective deepening) and cyclones (anomalous heat gain and restratification), so that it is not unreasonable that the averaged effect is captured by our calculation.
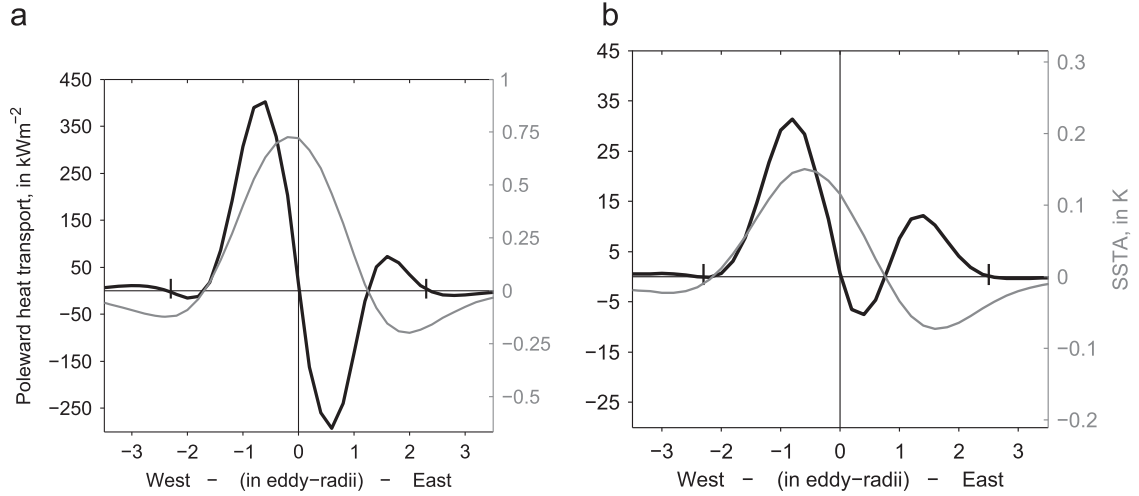
5.2. Swirl heat transport

The swirl meridional velocity field in (6) is estimated, using geostrophy, from the distribution of SSHA along the zonal section through the centre of the composites in Figs. 3a,b (energetic regions) and 5a,b (quiescent regions). That is, we use $\langle \delta v - v_d \rangle = \langle v_g' \rangle \equiv \langle (g/f_0) \partial \text{SSHA}/\partial x \rangle$, where $g = 9.81 \text{ m}^2 \text{ s}^{-1}$ is the gravity and f_0 is the local value of the Coriolis parameter. The temperature perturbation δT in (6) is likewise estimated from the SSTA composites $\langle T' \rangle$ shown in the same Figures. In the following an average eddy perturbation is obtained by further compositing panels a and b of Figs. 3 and 5 (i.e. from composite averages taken over all snapshots of both anticyclones and cyclones, after multiplying the latter by -1).

Using these composites and the assumptions discussed in Section 5.1, the swirl heat transport due to an average eddy is estimated as

$$H_{swirl}/\overline{n} = \rho_0 c_p \langle \overline{h}_{ml} \rangle \int_0^{L_x} \langle v_g' \rangle \langle T' \rangle \, dx. \qquad (8)$$

Local surface transports $\rho_0 c_p \langle v_g' \rangle \langle T' \rangle$ are displayed in Fig. 6. In both energetic (Fig. 6a) and quiescent regions (Fig. 6b), they peak on the western side of the eddy centre. In energetic regions this peak in poleward heat transport reaches more than 300 kW m^{-2}, an order of magnitude more than in quiescent regions, where transport peaks at roughly 30 kW m^{-2}. Over the nearly in-phase warm anticyclones and cold cyclones observed in energetic regions (Fig. 6a), the flow on the eastern eddy side returns a large part of this heat equatorward. In contrast, over quiescent regions' eddies (Fig. 6b), the eastern return flow mostly contributes to the poleward transport of heat, a consequence of the larger westward phase shift observed between their SSTA and SSHA. These differences emphasize the presence of larger rotational heat fluxes (e.g. Marshall and Shutts, 1981) in energetic compared to quiescent regions (see also Appendix B).

To obtain the net heat transport due to an average eddy, the integral in (8) is computed over a length L_x taken in such a way that the mass transport $\int_0^{L_x} \langle v_g' \rangle \, dx = 0$. This "eddy wavelength" is shown by the short vertical bars in Fig. 6 and typically extends

Fig. 6. Poleward heat transport at the surface due to eddy swirl, $\rho c_p \langle v_g' \rangle \langle T' \rangle$, in energetic (a) and quiescent regions (b). Note the different scales. Composite eddy SSTA is also shown (as both-polarity average, after multiplying cyclonic sections by -1).

Table 2
Eddy poleward mixed-layer heat transport.

			Energetic		Quiet	
			GS	ACC	NA	SP
1.	$\overline{n}$		24 ± 3	169 ± 11	54 ± 6	72 ± 6
2.	$H_{swirl}/\overline{n}$	in TW	2.2	1.3	.2	.2
			(3.3)	(2.0)	(.3)	(.3)
3.	H_{swirl}	in PW	$.05 \pm .007$	$.23 \pm .015$	$.01 \pm .001$	$.01 \pm .001$
			$(.08 \pm .011)$	$(.34 \pm .023)$	$(.01 \pm .002)$	$(.02 \pm .002)$
4.	$H_{drift}/\overline{n}$	in TW	.01	.12	$\times$	$\times$
			(.01)	(.14)		
5.	H_{drift}	in PW	$.00 \pm .000$	$.02 \pm .001$	$\times$	$\times$
			$(.00 \pm .000)$	$(.02 \pm .002)$		
6.	$H_{drift} + H_{swirl}$	in PW	$.05 \pm .007$	$.24 \pm .017$	$.01 \pm .001$	$.01 \pm .001$
			$(.08 \pm .011)$	$(.36 \pm .025)$	$(.01 \pm .002)$	$(.02 \pm .002)$
7.	κ	in m^2 s^{-1}	2900	1200	900	400
			(4300)	(1800)	(1400)	(600)

For eddies with origins in energetic regions of Gulf Stream (GS) and ACC, and quiet regions of North Atlantic (NA) and South Pacific (SP). See text for details. Values in parentheses are corrected for a systematic low bias (at $\frac{n-1}{n} \simeq 0.8$) in eddy composites of T' (and v_g'), as detailed in Appendix A.

across ≈ 5 eddy radii. Table 2 (row 2) gives the values of $H_{swirl}/\overline{n}$ for the composites of the different regions. It shows that a single eddy found in energetic regions transports on average $\approx 10^{12}$ W poleward in the mixed-layer, an order of magnitude more than a single eddy in quiescent regions ($\approx 10^{11}$ W).

To scale these numbers up to the basin, we multiply by the average number of eddies, $\overline{n}$, that coexist at a given time in each region (given in Table 2, row 1). As shown in Table 2 (row 3), this yields a net poleward mixed-layer eddy heat transport H_{swirl} of 0.05 PW across the Gulf Stream, 0.2 PW across the ACC and 0.01 PW across the quiet regions of the North Atlantic and South Pacific. Assuming that the principal source of uncertainty is the number of coexisting eddies, the variability between different weeks provides an estimate of the uncertainty of the eddy heat transports, which is found to be on the order of 10% (see Table 2, rows 1 and 3).

5.3. Drift heat transport

The drift heat transport of an average eddy is estimated from (7) as:

$$H_{drift}/\overline{n} = \rho_0 c_p \langle \overline{h}_{ml} \rangle \int_0^{L_x} \langle v_d \rangle \langle T' \rangle \, dx, \qquad (9)$$

in which L_x and $\langle T' \rangle$ are the same as in (8).

The average eddy drift velocity $\langle v_d \rangle$ in (9) is simply estimated from meridional track displacements. The composites of the resulting meridional track velocity $\langle v \rangle$ are displayed in Fig. 7 (continuous lines) for cyclones ($\langle v \rangle^C$, in grey) and anticyclones ($\langle v \rangle^A$, in black) as function of the eddy lifetime, and are compared, for reference, to the composites of the cross isotherm velocity v_T (dashed lines, estimated by projecting the track velocity onto the time-mean SST gradient). To assure mass conservation, that is to eliminate a net meridional eddy transport or advection of tracks by the mean-flow, the eddy drift velocity is estimated as $\langle v_d \rangle = (\langle v \rangle^A - \langle v \rangle^C)/2$ (i.e. as half the difference between black and grey curves in Fig. 7), whose lifetime-average is used in (9).

Fig. 7a shows that warm anticyclones originating in energetic regions of the Gulf Stream and the ACC move poleward and towards colder waters with a velocity $|v| \approx |v_T| \approx 0.5$ cm/s in the first months of their lifetime, and conversely, that cold cyclones move equatorward and towards warmer water at a similar rate. Here the net eddy (mass) transport velocity ($\langle v \rangle^A + \langle v \rangle^C$) is indeed only a small residual of the recirculating eddy drift $\langle v_d \rangle$, both branches of which add up in terms of heat transport and lead to a net eddy transport of heat poleward.

In quiescent regions (Fig. 7b), in contrast, eddies move equatorward and "warm-ward" irrespective of their temperature/height signal, and do so at different rates ($v \neq v_T$). The net equatorward
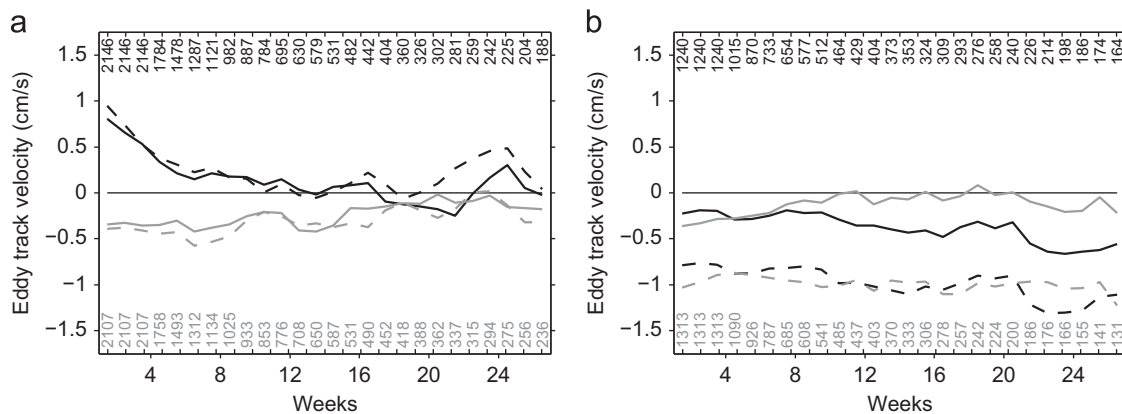
Fig. 7. Observed meridional (solid) and cross-isotherm (dashed) eddy track velocity throughout the life-time of anticyclones (black) and cyclones (grey) with origins in energetic (a) and quiet regions (b). Positive values indicate propagation towards colder surface waters or higher latitudes. As eddies die, decreasing eddy numbers contribute to the average (indicated at the top/bottom of the panels for anticyclones/cyclones).

translation, possibly in the form of advection by the gyre mean-flow (see also CSS11), dominates track displacements, with the drift being only a small residual. Therefore, we do not further quantify the associated drift heat transport here.

To evaluate (9), $\langle v_d \rangle$ is assumed uniform within the eddy core, defined as the closed zero-contour in the SSHA composites,[4] and is set to zero outside. For reference, the mixed-layer heat anomaly within an eddy core $\delta q \equiv \rho_0 c_p \langle \overline{h}_{ml} \rangle \iint_{core} \langle T' \rangle \, dS$, is $\approx 0.34 \times 10^{19}$ J for a typical GS eddy. The composite ACC eddy heat anomaly ($\approx 0.45 \times 10^{19}$ J) is larger (primarily a result of deeper mixed-layers in the Southern Ocean) and at the lower end of in-situ estimates for the *depth-integrated* heat content of eddies previously observed along the ACC (ranging from 0.8 to 5.4×10^{19} J – see Joyce et al., 1981; Morrow et al., 2004; Peterson et al., 1982; Swart et al., 2008).

Application of (9) provides the numbers for $H_{drift}/\overline{n}$ given in Table 2, row 4. After multiplication by $\overline{n}$, the total drift heat transport (Table 2, row 5) is found to be near zero (only 0.25% of the swirl) in the Gulf Stream region, where a systematic drift is only observed in the first month of the eddy lifetime (with a lifetime-average $\langle v_d \rangle \approx 0$), and contributes only a fraction of the swirl heat transport ($\leq 10\%$) in the ACC, where $\langle v_d \rangle \approx 0.3$ cm s^{-1}.

The implication of this calculation is that the eddies seen by the altimeter in energetic regions carry heat in the mixed layer primarily as a result of the small phase shift between their pressure and temperature centres, not as a result of their meridional drift. Put differently, even though the casual observation of Gulf Stream or ACC meanders pinching-off in satellite SST maps is suggestive of heat transport by eddy shedding, the associated drift velocity is not large enough to contribute significantly to the heat transport. Rather, it is the fact that the warm and cold cores are not actually centred on the pressure cores, but slightly displaced to the west, which predominately leads to eddy heat transport in the mixed-layer.[5]

Although our focus is on the upper mixed layer, it is interesting to speculate on the relative contributions of drift and swirl heat transports to the column averaged heat transport. Indeed, while the swirl heat transport is likely primarily restricted to the mixed layer, consistent with the decrease of the phase shift with depth observed in the North Pacific (Qiu and Chen, 2005; Roemmich and Gilson, 2001), drifting warm and cold eddy cores

extend through the thermocline (≈ 1 km). As a result, it is possible that the two contributions to the depth-integrated eddy heat transport become more comparable over the ACC.

5.4. Total eddy heat transport

The total eddy heat transport is obtained by summing the numbers from Sections 5.2 and 5.3 (Table 2, row 6—only the swirl heat transport is included for quiescent regions, as discussed above). Eddies in quiescent regions transport a very modest amount of heat poleward in the mixed layer (≈ 0.01 PW), which, as expected, contrasts with the larger numbers found over the GS (0.05 PW), and the ACC (0.24 PW).

Correcting for a systematic low bias (see Appendix A) in eddy composites of both T' and v_g', leads to the numbers given in parentheses below the original numbers in Table 2. They are enhanced by a factor $(n/n-1)^2 \simeq 1.5$ for the swirl heat transport, whereas the drift heat transport is only enhanced by $(n-1/n)^1 \simeq 1.2$, as the bias on eddy tracks, and thus v_d, is unknown.

The heat transport calculation, presented here, is based on observations of eddies originating from a broad range of latitudes[6] and only applies to the surface mixed-layer. As a result, a direct comparison to previous estimates of zonally and depth-integrated eddy heat transport is only tentative. Nevertheless, a range of observational studies indicate a strong surface intensification of eddy heat transports in the ACC and mid-latitudes (Phillips and Rintoul, 2000; Qiu and Chen, 2005; Roemmich and Gilson, 2001; Wunsch, 1999). In light of this, it is interesting to note that the heat transported in the surface mixed-layer (≈ 100 m) by propagating eddies originating in the energetic ACC region, which is almost entirely provided by the eddy swirl component ($H_{swirl} + H_{drift} \approx H_{swirl} \approx 0.3$ PW), lies within the range of previous estimates for the total, depth-integrated, cross-ACC eddy heat transport (0.1 to 0.9 PW, as summarized by Gille, 2003). It thus provides a substantial fraction of the eddy heat transport required to close the oceanic heat-budget poleward of the ACC, consistent with the 0.45 ± 0.3 PW estimate by de Szoeke and Levine (1981).

Finally, it is worth emphasizing that the ACC dominates the numbers in Table 2 (row 6) only due to its large zonal extent. Here, an individual eddy transports on average only 60% of the

---

[4] This likely overestimates the region, in which eddies carry water parcels and which is better approximated by the zero-contour in relative vorticity (Early et al., 2011). Results are however not very sensitive to this definition, as smaller cores are compensated by larger core-average $\langle T' \rangle$.

[5] As pointed out by a reviewer, there is also certainly a geographical constraint on the extent of meridional motions by eddies near the Gulf Stream.

[6] Note that the NA energetic region, referred to as GS in the Tables, also includes $\approx 8\%$ of tracks with origins in the Mexican Loop Current (see also Figs. 1 and 2).

heat a GS eddy transports in the mixed-layer, even though mixed-layers are typically twice as deep over ACC eddies. Appendix B sheds further light on this interesting discrepancy.

5.5. Implied diffusivities

For reference and comparison with other studies, a bulk diffusivity κ for the poleward mixed-layer heat transport by eddies in a given region can be estimated from the relation

$$\frac{(H_{swirl}+H_{drift})/\overline{n}}{\rho c_p \langle \overline{h}_{ml} \rangle L_x} = \frac{1}{L_x}\int_0^{L_x}(\langle v'_g \rangle + \langle v_d \rangle)\langle T' \rangle\, dx$$

$$= -\kappa \left\langle \frac{\partial \overline{T}}{\partial y} \right\rangle, \tag{10}$$

in which we have used (8) and (9). In this equation, $\langle \partial \overline{T}/\partial y \rangle$ is the meridional gradient of the monthly SST climatology, evaluated and averaged along eddy tracks. (Note that for the quiescent regions, again, the drift heat transport is not included.)

The resulting diffusivities are found to be relatively modest in quiescent regions. In the South Pacific, where $\langle \partial \overline{T}/\partial y \rangle = -0.5$ K/100 km, one obtains $\kappa \approx 500$ m^2 s^{-1}. Larger diffusivities are found in the NA subtropics ($\kappa \approx 900$ m^2 s^{-1}), where the north–south tilting of isotherms leads to a meridional temperature gradient of only -0.2 K/100 km.

The SST gradient averaged over ACC and GS eddies is of the same order as in the quiescent regions (-0.8 K/100 km), but because of much larger values of H_{swirl} in energetic regions, diffusivities are larger (≈ 1200 m^2 s^{-1} for the ACC and 2900 m^2 s^{-1} for the GS – or, after bias correction, ≈ 1800 and > 4000 m^2 s^{-1}, respectively). These numbers (summarized in Table 2, row 7) are broadly consistent with the spatial distribution of κ estimated from altimetry (Stammer, 1998). In particular, they closely agree with the larger values of κ observed over the GS core by Zhai and Greatbatch (2006). The weaker values observed here in the energetic ACC region likely reflect a combination of weak diffusivities in the ACC core and larger diffusivities in the western boundary current extensions (Agulhas return current and Brazil-Malvinas confluence) on its equatorward flank (as estimated by e.g. Marshall et al., 2006).

Apart from a 100 m^2 s^{-1} contribution by the drift mechanism in the ACC, diffusivities and their observed regional variations entirely reflect the eddy swirl. Appendix B provides some insight into the physical mechanisms at work.

6. Conclusion

The goal of this study was to determine empirically the signature in SST of the mesoscale eddy field and compute the associated heat transport, through an analysis of the relationship between SST and SSH at fixed-location and directly following eddy tracks. Our key results can be summarized as follows:

- Propagating eddies indeed have a clear signature in SST. This conclusion is not restricted to the regions of high σ_{SSHA}, associated with major current systems, but also applies to quiescent oceanic interiors.
- The eddy SST signature is characterized by warm anticyclones and cold cyclones, but also by a westward phase shift of SSTA with respect to rotating eddy cores. This phase shift is more pronounced for eddies originating in quiescent regions of the subtropical gyres, but is also clearly established for the GS and ACC regions.
- The spatial phase shift between temperature and pressure signals of an eddy is such that it implies a systematic poleward eddy heat transport in the mixed layer. This mechanism of

"swirl" heat transport is found to be particularly significant over the ACC region (≈ 0.2 PW) and dominates over the "drift" heat transport associated with the poleward motion of warm anticyclones and the equatorward motion of cold cyclones over the ACC and the GS regions.

It is striking to observe westward phase shifts, reminiscent of linear unstable baroclinic disturbances, over tracked eddies whose dynamics have been shown to be nonlinear (CSS11) and whose radii are larger than the observed most baroclinically unstable scale (Smith, 2007; Tulloch et al., 2011). Since they are most likely generated by baroclinic instability, eddies must evolve through an inverse energy cascade while conserving their SSTA–SSHA phase relationship. As such they appear to transport heat poleward in two stages. First, by extracting available potential energy from the environment during the initial stage of their growth (on the order of 10 days for energetic regions according to Tulloch et al., 2011), a behaviour captured by classical models of baroclinic instability (e.g. Eady, 1949). Second, by subsequently cascading to larger scale and continuing to transport heat poleward, a behaviour that is reminiscent of the archetypal "heton" heat transport model introduced by Hogg and Stommel (1985).

The observed phase shift between pressure and temperature has been shown here to be the key mechanism by which mesoscale motions transport heat poleward in the mixed layer. It is unclear at this stage whether there is a single dominant mechanism that sets this phase shift (e.g. as proposed for the similar eddy signatures observed in Chlorophyll by Chelton et al., 2011a), or whether it reflects an intricate balance between horizontal stirring, entrainment of subsurface waters and heat exchanges with the atmosphere on mesoscales (whose important role in the general circulation is starting to be widely appreciated Cerovečki and Marshall, 2008; Greatbatch et al., 2007; Shuckburgh et al., 2011). Further observational and modelling studies will hopefully shed light on these fascinating issues.

Appendix A. Systematic and random biases in estimated eddy composite anomalies

Estimating the SST signature of propagating eddies by composite averaging along eddy tracks is only imperfect. First, there is variability in SST associated with processes other than the mesoscale circulation of interest here (e.g. atmospheric forcing via Ekman advection and surface heat exchange). These, as well as AMSR-E measurement errors, induce essentially random errors, which can be greatly reduced by averaging over many tracks and measurements. Second, the fact that SST perturbations are evaluated with respect to an imperfect estimate of the seasonal background state induces additional biases. As shown below, these are not

purely random, but also contain a systematic component, which is not reduced by considering a large number of tracks.

To see this, consider the hypothetical case in which we have n years of observations at a given location and only during the last of those a warm eddy, characterized by a SST perturbation δT_o, passes. The empirical estimate of the seasonal cycle $\overline{T}_{obs}$, obtained as described in Section 2, then yields

$$\overline{T}_{obs} = \overline{T} + \frac{0 + \cdots + 0 + \delta T_o}{n} = \overline{T} + \frac{\delta T_o}{n}, \qquad (A.1)$$

which differs from $\overline{T}$, the true seasonal cycle. The true temperature anomaly T' at the given location along the track is by definition equal to δT_o,

$$T' \equiv T - \overline{T} = \delta T_o \qquad (A.2)$$

However the empirical estimate is only

$$T'_{obs} \equiv T - \overline{T}_{obs} = (T' + \overline{T}) - \overline{T}_{obs} = \frac{n-1}{n}\delta T_o < \delta T_o, \qquad (A.3)$$

after use of (A.1) and (A.2). For a finite observational time series of length n (in years), we thus expect to underestimate the true eddy signature in SST by the factor $(n-1)/n$.

To account for more realistic situations, in which eddies can pass a given location in all years and also to account for non-eddy variability, we generate synthetic data of T along the tracks of propagating eddies and estimate the composite average in the same way as we do for the observations (Section 4). All tracks are chosen to be of 16-week duration (a relatively short duration, which gives a more stringent test), and are described by the coordinate $s(x,y,t)$, which follows each track in time and space. In this more general case, the empirical estimate of the seasonal cycle along a track, from (A.1), becomes:

$$\overline{T}_{obs}(s) = \overline{T}(s) + \frac{1}{n}\sum_{yr=1}^{n} T'(s + (0,0,yr)), \qquad (A.4)$$

where yr is the time-coordinate in years and the notation $s + (0,0,yr)$ indicates the same location on a given track. The observed temperature anomaly along the track, introduced by (A.3), is thus given by:

$$T'_{obs}(s) \equiv T(s) - \overline{T}_{obs}(s) = T'(s) - \frac{1}{n}\sum_{yr=1}^{n} T'(s + (0,0,yr)), \qquad (A.5)$$

in which both the passing of mesoscale eddies (T'_o), as well as atmospheric forcing (T'_a) contribute to the true temperature anomaly along the track ($T' = T'_o + T'_a$).

As in the simple example above, we assume that an eddy's temperature perturbation $T'_o(s) = \delta T_o$ is constant along its track and the same for all tracked eddies. The passing of eddies along the eddy track in the other $n-1$ years (i.e. at $s + (0,0,yr)$), also enters the estimate of T'_{obs} (from the second term in (A.5)), and is simulated as

$$T'_o(s + (0,0,yr)) = \delta T_o \sum_{i=1}^{3} \cos(\Lambda(yr)ks + \Phi(i)). \qquad (A.6)$$

Here the summation over three "waves" with random phase Φ reflects variation in the eddy polarity (warm or cold eddies) and amplitude (0 to $3\,\delta T_o$), and for each year (yr) a random process determines whether eddies propagate along the track ($\Lambda = 0$) or across ($\Lambda = 1$). In the latter case, the along-track wavelength $2\pi/k$ is set to 6 weeks (larger k are unrealistic given the observed eddy widths and propagation speeds, and for smaller k we essentially recover the case $\Lambda = 0$).

The atmospherically forced SST variability T'_a is assumed to be correlated in space along each entire eddy track. It thus reduces to a temporal anomaly in the area traversed by the eddy. As is typical in such problems (e.g. Frankignoul, 1985), we simulate the

associated time series as a first order autoregressive process (AR-1), with a decorrelation time of 4 months. The standard deviation of this process is denoted by $\sigma(T'_a)$ and, together with the number of tracks considered, is chosen as a controlling parameter in these simulations. The AR-1 model and (A.6) determine the anomalies in (A.5) along an arbitrary number of tracks. Their weekly snapshots are then composite-averaged to obtain $\langle T'_{obs} \rangle$, as was done in Section 4 for the SST and SSH data.

Fig. A1 displays the mean, along with upper and lower 5 percentiles, of $\langle T'_{obs} \rangle$ as a function of the number of tracks considered, based on a thousand independent realizations of the random processes described above for T'_o and T'_a. Dashed, black and grey curves display three different experiments, for which the ratio $\sigma(T'_a)/\delta T_o$ is set to 0, 1 and 5, respectively. The case $\sigma(T'_a)/\delta T_o = 0$ represents the ideal situation, in which no atmospheric forcing is present. As seen in Fig. A1 (dashed curves), the normalized composite $\langle T'_{obs} \rangle/\delta T_o$ then rapidly approaches the limit $n-1/n \approx 0.82$ for $n = 5.5$ (half the tracks with 5 years, half with 6 years, composited in random order). Indeed, in 90% of realizations, the normalized composite is bounded by $\pm 2\%$ of this value, when more than 1000 tracks are composited. The enhanced spread in the black and grey lines in Fig. A1 reflects masking of the eddy signal by atmospherically forced variability (term 1 in (A.4)), which also enhances the random bias in the estimated background seasonal state (term 2 in (A.4)). Here, in 90% of cases, the normalized eddy composite $\langle T'_{obs} \rangle/\delta T_o$ lies within $\pm 5\%$ (for $\sigma(T'_a)/\delta T_o = 1$, black) and 25% (for $\sigma(T'_a)/\delta T_o = 5$, grey) of $n-1/n$ once more than a thousand tracks are considered. (Note that in both cases the atmospherically forced variability present in individual eddy snapshots is reduced by more than 95% in the eddy composite, i.e. $\langle T'_a \rangle/\sigma(T'_a) < 0.05$.)

In summary, the observed composites systematically underestimate the true observed eddy perturbation by the factor $n-1/n$. At the 90% confidence interval, they lie within a narrow error margin around this value, both for SSHA ($< 2\%$, likened to the $\sigma(T'_a)/\delta T_o = 0$ experiment since the large-scale steric to eddy SSHA variance ratio is observed to be small) and for SSTA in energetic regions ($< 5\%$ for the 2000 tracks typically composited in these regions in Section 4, taking the $\sigma(T'_a)/\delta T_o = 1$ experiment to be the relevant regime since observed SSTA have comparable large-scale and mesoscale variance in energetic
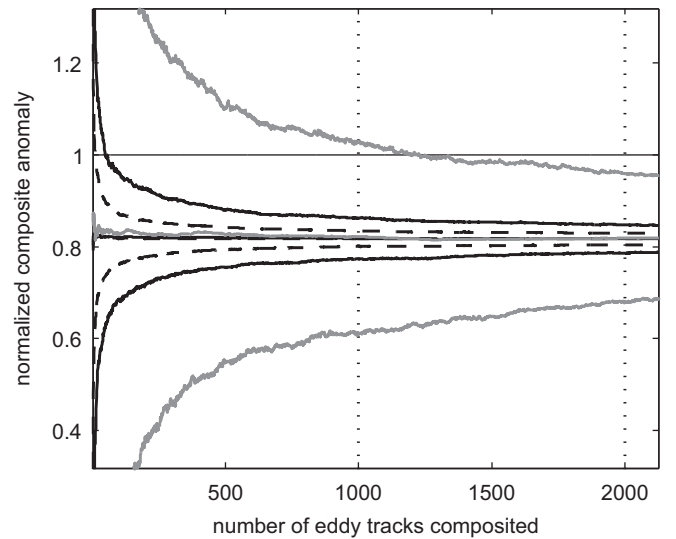
Fig. A1. 1000 realization average, and upper/lower 5 percentiles, of the observed composite $\langle T'_{obs} \rangle$, normalized by δT_o, for three different experiments: $\sigma(T'_a)/\delta T_o = 0$ (dashed), 1 (black) and 5 (grey). As the number of tracks composited increases (abscissa), $\langle T'_{obs} \rangle/\delta T_o$ converges towards its expected value $n-1/n$ (≈ 0.8). The vertical dashed lines indicate the typical number of tracks considered in our study.

regions). The $\sigma(T'_a)/\delta T_0 = 5$ is the relevant regime for SSTA composites in quiescent regions. Their larger error margins ($< 25\%$ for > 1000 tracks composited, and the hard set of parameters chosen here) reflect the imperfect averaging out of large-scale atmospherically forced variability predominating the SSTA variance in these regions.

Appendix B. More on diffusivities

As shown in Section 5.5, the meridional mixed-layer eddy diffusivity for heat κ is almost entirely provided by the eddy swirl (given by the first term in (10)). To gain insight into the mechanisms that set the observed regional differences in this predominant component of κ, we introduce a typical scale v_0 for $\langle v'_g \rangle$, T_0 for $\langle T' \rangle$, and a typical length scale $L_0 \equiv -T_0 / \langle \partial \overline{T} / \partial y \rangle$. With these new variables, the swirl diffusivity can be expressed as

$$\kappa = c_e v_0 L_0. \tag{B.1}$$

Here, the non-dimensional parameter

$$c_e \equiv \frac{1}{L_x} \int_0^{L_x} \frac{\langle v'_g \rangle \langle T' \rangle}{v_0 T_0} dx \tag{B.2}$$

measures the efficiency of the eddy heat transport. c_e is zero when eddy perturbations in temperature and velocity are in quadrature, and reaches its maximum when they are in phase (or, in terms of pressure, $c_e = 0$ when temperature and pressure fluctuations are in phase, and c_e is maximum when they are in quadrature). Thus c_e is a simple function of the phase shift between temperature and pressure, and the shape of this function is given for sinusoidal signals by the curves in Fig. B1 (continuous line for an infinite plane wave, dashed line for a localized wave-packet). Observed values of c_e and SSTA/SSHA phase shifts, obtained from eddy composites in different regions, are superimposed on these curves (to do so T_0 and v_0 are simply set to the average magnitude of the positive and negative extrema observed in $\langle T' \rangle$ and $\langle v'_g \rangle$, respectively). As can be seen, c_e is about three times larger in quiescent regions than in energetic regions. This regional variation in c_e reflects differences in the observed eddy SST signature, and if this were the sole effect (i.e. if it were not compensated by an increase in v_0 or L_0), it would lead to larger diffusivities in the quiescent regions away from major current systems.

The variability of v_0 and L_0 amongst the regions is as follows. In quiet regions, $L_0 \approx 30$ km, which is close to the local deformation scale or about a third of the observed eddy radius (≈ 80 km). In energetic regions of the GS and ACC, surface L_0 is enhanced to ≈ 60 km, which is more than twice as large as the deformation scale, or more than $\frac{2}{3}$ of the eddy radius. The velocity scale v_0 is found to be more than three times larger in energetic regions compared to quiet regions.

Combining these results reveals that the larger diffusivities observed over the GS compared to the ACC (see Section 5.5 and Table 2) result mainly from more vigorous eddies (larger v_0), but also from slightly larger mixing lengths (L_0) and efficiency c_e (see Fig. B1). Weaker eddies (v_0) with shorter mixing lengths (L_0) drive the reduction in κ from energetic to quiescent regimes. Interestingly, this reduction in κ is limited by the regional variations in the heat transport efficiency c_e: the spread between quiescent and energetic regimes would be three times larger, if c_e were a constant (as is often assumed in the literature, e.g. Holloway and Kristmannsson, 1984; Karsten and Marshall, 2002; Stammer, 1998; Visbeck et al., 1997; Wunsch, 1999). Although a detailed analysis of the mechanisms that set c_e is beyond the scope of this study, it is worth pointing out that, besides purely fluid dynamical effects such as those studied by Spall and Chapman (1998), interactions of eddies with the subsurface (through entrainment) and with the atmosphere (through turbulent air–sea heat flux damping) are likely to be important mechanisms to consider (see for example Greatbatch et al., 2007; Shuckburgh et al., 2011).

References

Auer, S.J., 1987. Five-year climatological survey of the Gulf Stream system and its associated rings. J. Geophys. Res. 92, 11709–11726.

Bretherton, F.P., 1982. Ocean climate modeling. Progr. Oceanogr. 11, 93–129.

Brown, O.B., Cornillon, P.C., Emmerson, S.R., Carle, H.M., 1986. Gulf Stream warm rings: a statistical study of their behavior. Deep-Sea Res. 33, 1459–1473.

Cerovečki, I., Marshall, J., 2008. Eddy modulation of air–sea interaction and convection. J. Phys. Oceanogr. 38, 65–83.

Chelton, D.B., Gaube, P., Early, J.J., Samelson, R.M., 2011a. The influence of nonlinear mesoscale eddies on near-surface oceanic Chlorophyll. Science 334, 328–332.

Chelton, D.B., Schlax, M.G., Freilich, M.H., Milliff, R.F., 2004. Satellite measurements reveal persistent small-scale features in ocean winds. Science 303, 978–983.

Chelton, D.B., Schlax, M.G., Samelson, R.M., 2011b. Global observations of nonlinear mesoscale eddies. Progr. Oceanogr. 91, 167–216.

Chelton, D.B., de Szoeke, R.A., Schlax, M.G., El Naggar, K., Siwertz, N., 1998. Geographical variability of the first baroclinic Rossby radius of deformation. J. Phys. Oceanogr. 28, 433–460.

Chelton, D.B., Wentz, F.J., 2005. Global microwave satellite observations of sea surface temperature for numerical weather prediction and climate research. Bull. Am. Meteorol. Soc. 86, 1097–1115.

Cipollini, P., Cromwell, D., Jones, M.S., Quartly, G.D., Challenor, P.G., 1997. Concurrent altimeter and infrared observations of Rossby wave propagation near 34°N in the northeast Atlantic. Geophys. Res. Lett. 24, 889–892.

Cornillon, P., Weyer, R., Flierl, G., 1989. Translational velocity of warm core rings relative to the slope water. J. Phys. Oceanogr. 19, 1317–1332.

Czaja, A., Blunt, N., 2011. A new mechanism for ocean-atmosphere coupling in midlatitudes. Q. J. R. Meteorol. Soc. 137, 1095–1101.

de Boyer Montégut, C., Madec, G., Fischer, A.S., Lazar, A., Iudicone, D., 2004. Mixed layer depth over the global ocean: an examination of profile data and a profile-based climatology. J. Geophys. Res. 109.

de Szoeke, R.A., Levine, M.D., 1981. The advective flux of heat by mean geostrophic motions in the Southern-Ocean. Deep-Sea Res. 28, 1057–1085.

Dewar, W.K., 1986. Mixed layers in Gulf Stream rings. Dynam. Atmos. Oceans 10, 1–29.

Dong, S., Gille, S.T., Sprintall, J., Gentemann, C., 2006. Validation of the Advanced Microwave Scanning Radiometer for the Earth Observing System (AMSR-E) sea surface temperature in the Southern Ocean. J. Geophys. Res. 111, C04002.

Ducet, N., Le Traon, P.Y., 2000. Global high-resolution mapping of ocean circulation from TOPEX/Poseidon and ERS-1 and 2. J. Geophys. Res. 105.

Eady, E.T., 1949. Long waves and cyclone waves. Tellus 1, 33–52.

Early, J.J., Samelson, R.M., Chelton, D.B., 2011. The evolution and propagation of quasigeostrophic ocean eddies. J. Phys. Oceanogr. 41, 1535–1555.

Frankignoul, C., 1985. Sea surface temperature anomalies, planetary waves and air–sea feedback in the middle latitudes. Rev. Geophys. 23, 357–390.
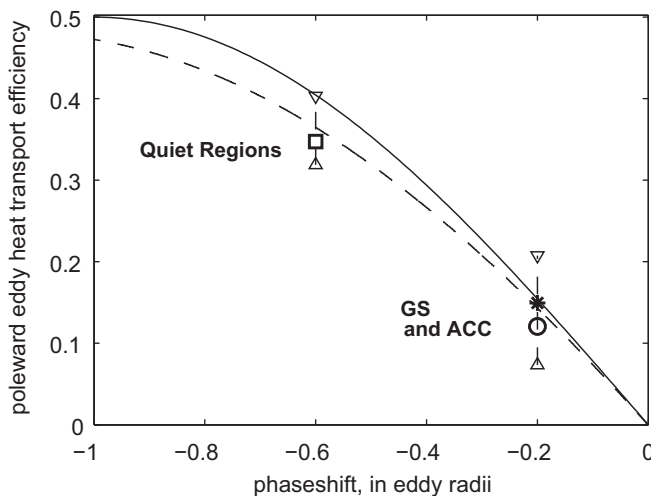
Fig. B1. The efficiency c_e of the poleward mixed-layer eddy heat transport, from (B.2), observed over eddies in quiescent regions □, Gulf Stream (∗) and ACC (o). As for a plane wave (solid line) or a localized wave-packet (dashed line), c_e is a simple function of the phase shift δ_x between eddy SSTA and SSHA. (The differences in c_e, observed between oceanic regimes, clearly stand out from the error on c_e, which is associated to the observed accuracy in δ_x of ± 0.1 eddy radii, indicated by dashed vertical lines and estimated from the slope of the dashed curve).

Gentemann, C.L., Donlon, C.J., Stuart-Menteth, A., Wentz, F.J., 2003. Diurnal signals in satellite sea surface temperature measurements. Geophys. Res. Lett. 30, 1140.

Gille, S.T., 2003. Float observations of the Southern Ocean. Part II: Eddy fluxes. J. Phys. Oceanogr. 33, 1182–1196.

Greatbatch, R.J., Zhai, X., Eden, C., Olbers, D., 2007. The possible role in the ocean heat budget of eddy-induced mixing due to air–sea interaction. Geophys. Res. Lett. 34.

Halliwell, G.R., Mooers, C.N.K., 1979. The space-time structure and variability of the shelf water-slope water and Gulf Stream surface temperature fronts and associated warm-core eddies. J. Geophys. Res. 84, 7707–7725.

Halliwell, G.R., Ro, Y.J., Cornillon, P., 1991. Westward-propagating sst anomalies and baroclinic eddies in the Sargasso Sea. J. Phys. Oceanogr. 21, 1664–1680.

Hogg, N.G., Stommel, H.M., 1985. The heton, an elementary interaction between discrete baroclinic geostrophic vortices and its implications concerning eddy heat-flow. Proc. R. Soc. Lond. A. Math. Phys. Sci. 397, 1–20.

Holloway, G., Kristmannsson, S.S., 1984. Stirring and transport of tracer fields by geostrophic turbulence. J. Fluid Mech. 141, 27–50.

Jayne, S.R., Marotzke, J., 2002. The oceanic eddy heat transport. J. Phys. Oceanogr. 32, 3328–3345.

Joyce, T.M., Patterson, S.L., Millard Jr., R.C., 1981. Anatomy of a cyclonic ring in the Drake Passage. Deep-Sea Res. 28, 1265–1287.

Karsten, R.H., Marshall, J., 2002. Constructing the residual circulation of the ACC from observations. J. Phys. Oceanogr. 32, 3315–3327.

Leeuwenburgh, O., Stammer, D., 2001. The effect of ocean currents on sea surface temperature anomalies. J. Phys. Oceanogr. 31, 2340–2358.

Lentini, C.A.D., Olson, D.B., Podestá, G.P., 2002. Statistics of Brazil Current rings observed from AVHRR: 1993 to 1998. Geophys. Res. Lett. 29, 1811.

Marshall, J., Jones, H., Karsten, R., Wardle, R., 2002. Can eddies set ocean stratification? J. Phys. Oceanogr. 32, 26–38.

Marshall, J., Jones, H., Karsten, R., Wardle, R., 2006. Estimates and implications of surface eddy diffusivity in the Southern Ocean derived from tracer transport. J. Phys. Oceanogr. 36, 1806–1821.

Marshall, J., Shutts, G.J., 1981. A note on rotational and divergent eddy fluxes. J. Phys. Oceanogr. 11, 1677–1680.

Minobe, S., Kuwano-Yoshida, A., Komori, N., Xie, S.P., Small, R.J., 2008. Influence of the Gulf Stream on the troposphere. Nature 452, 206-U51.

Morrow, R., Donguy, J.R., Chaigneau, A., Rintoul, S.R., 2004. Cold-core anomalies at the subantarctic front, south of Tasmania. Deep-Sea Res. Pt I 51, 1417–1440.

Park, K.A., Cornillon, P., Codiga, D.L., 2006. Modification of surface winds near ocean fronts: effects of Gulf Stream rings on scatterometer (QuikSCAT, NSCAT) wind observations. J. Geophys. Res. 111.

Pascual, A., Faugère, Y., Larnicol, G., Le Traon, P.Y., 2006. Improved description of the ocean mesoscale variability by combining four satellite altimeters. Geophys. Res. Lett. 33.

Peterson, R.G., Nowlin, W.D., Whitworth, T., 1982. Generation and evolution of a cyclonic ring at Drake Passage in early 1979. J. Phys. Oceanogr. 12, 712–719.

Phillips, H.E., Rintoul, S.R., 2000. Eddy variability and energetics from direct current measurements in the Antarctic Circumpolar Current south of Australia. J. Phys. Oceanogr. 30, 3050–3076.

Qiu, B., Chen, S., 2005. Eddy-induced heat transport in the subtropical North Pacific from Argo, TMI, and altimetry measurements. J. Phys. Oceanogr. 35, 458–473.

Rahmstorf, S., Willebrand, J., 1995. The role of temperature feedback in stabilizing the thermohaline circulation. J. Phys. Oceanogr. 25, 787–805.

Rhines, P.B., Young, W.R., 1982. Homogenization of potential vorticity in planetary gyres. J. Fluid Mech. 122, 347–367.

Richardson, P.L., Maillard, C., Stanford, T.B., 1979. The physical structure and life history of cyclonic Gulf Stream ring Allen. J. Geophys. Res. 84, 7727–7741.

Ring Group, 1981. Gulf Stream cold-core rings: their physics, chemistry, and biology. Science 212, 1091–1100.

Roemmich, D., Gilson, J., 2001. Eddy transport of heat and thermocline waters in the North Pacific: a key to interannual/decadal climate variability? J. Phys. Oceanogr. 31, 675–687.

Shuckburgh, E., Maze, G., Ferreira, D., Marshall, J., Jones, H., Hill, C., 2011. Mixed layer lateral eddy fluxes mediated by air–sea interaction. J. Phys. Oceanogr. 41, 130–144.

Small, R.J., de Szoeke, S.P., Xie, S.P., O'Neill, L., Seo, H., Song, Q., Cornillon, P., Spall, M., Minobe, S., 2008. Air–sea interaction over ocean fronts and eddies. Dyn. Atmos. Oceans 45, 274–319.

Smith, K.S., 2007. The geography of linear baroclinic instability in earth's oceans. J. Mar. Res. 65, 655–683.

Song, Q., Cornillon, P., Hara, T., 2006. Surface wind response to oceanic fronts. J. Geophys. Res. 111, C12006.

Song, Q., Hara, T., Cornillon, P., Friehe, C.A., 2004. A comparison between observations and MM5 simulations of the marine atmospheric boundary layer across a temperature front. J. Atmos. Oceanic Technol. 21, 170–178.

Spall, M.A., Chapman, D.C., 1998. On the efficiency of baroclinic eddy heat transport across narrow fronts. J. Phys. Oceanogr. 28, 2275–2287.

Stammer, D., 1998. On eddy characteristics, eddy transports, and mean flow properties. J. Phys. Oceanogr. 28, 727–739.

Swart, N.C., Ansorge, I.J., Lutjeharms, J.R.E., 2008. Detailed characterization of a cold antarctic eddy. J. Geophys. Res. Oceans 113.

Sweet, W., Fett, R., Kerling, J., La Violette, P., 1981. Air–sea interaction effects in the lower troposphere across the North Wall of the Gulf Stream. Mon. Weather Rev. 109, 1042–1052.

Tulloch, R., Marshall, J., Hill, C., Smith, K.S., 2011. Scales, growth rates, and spectral fluxes of baroclinic instability in the ocean. J. Phys. Oceanogr. 41, 1057–1076.

Visbeck, M., Marshall, J., Haine, T., Spall, M., 1997. Specification of eddy transfer coefficients in coarse-resolution ocean circulation models. J. Phys. Oceanogr. 27, 381–402.

Voorhis, A.D., Schroeder, E.H., Leetmaa, A., 1976. The influence of deep mesoscale eddies on sea surface temperature in the North Atlantic subtropical convergence. J. Phys. Oceanogr. 6, 953–961.

Williams, R.G., 1988. Modification of ocean eddies by air–sea interaction. J. Geophys. Res. Oceans 93, 15523–15533.

Wunsch, C., 1999. Where do ocean eddy heat fluxes matter? J. Geophys. Res. Oceans 104, 13235–13249.

Zhai, X., Greatbatch, R.J., 2006. Inferring the eddy-induced diffusivity for heat in the surface mixed layer using satellite data. Geophys. Res. Lett. 33.